Data-driven and physics-based methods to optimize structures against delamination

Tota Rakesh Kumar[a,b,*], Marco Paggi[a]

[a] *Computational Mechanics Group, Research Unit MUSAM – Multi-scale Analysis of Materials, IMT School for Advanced Studies Lucca, Piazza San Francesco, 19, 55100, Lucca, Italy*
[b] *School of Marine Engineering and Technology, Indian Maritime University, Chennai, 600119, Tamil Nadu, India*

Abstract

Composite materials and multi-material components often fail at their internal interfaces/adhesive joints, and hence special attention should be given to such catastrophic delamination events to guarantee the system's functional requirements. So far, however, the majority of structural topology optimization problems have focused on optimal distribution of the bulk materials by considering interfaces as perfectly bonded. This motivates the introduction of optimization methods that explicitly take into account the role of the material interfaces to optimize structures against delamination. In this work, we propose a data-driven heuristic optimization approach for the identification of optimal cohesive interfaces with linearly graded fracture properties to increase the ability of the composite structure to withstand peeling. Moreover, for given cohesive interface properties, we investigate the applicability of the physics-based Solid Isotropic Material with Penalty (SIMP) topology optimization approach to optimize the internal structure of a substrate in problems where the stress field is affected by interface delamination.

Keywords: Cohesive fracture, Joining technologies, Graded interfaces, Particle swarm optimization, SIMP topology optimization.

*Corresponding author

Email addresses: totarakesh.kumar@imtlucca.it (Tota Rakesh Kumar), totarakeshk@imu.ac.in (Tota Rakesh Kumar), marco.paggi@imtlucca.it (Marco Paggi)

[0]This article is dedicated to the memory of Prof. Kaspar J. Willam (1940-2024), former Emeritus Professor at the University of Houston (USA), for his work on cohesive interface modelling and fracture mechanics and the kind discussion with the last author that have truly inspired his research since the first time they met in Vail, Colorado (USA), in occasion to the IA-FraMCoS-5 Congress in 2004.

Nomenclature

Acronyms

2D	two dimensional space
CZI	Cohesive zone interface
CZM	Cohesive zone model
FEA	finite element analysis
FEM	finite element method
PSO	particle swarm optimization
SIMP	Solid Isotropic Material with Penalization
TO	Topology Optimization

Variable notation

K	stiffness
$\mathscr{Z}$	PSO target cost function
ν	Poisson ratio
σ_n	normal traction
τ_t	tangential traction
E	Young's modulus
g_{n_c}	critical normal gap
g_{t_c}	critical tangential gap
u	displacement field

1. Introduction

Material components are often bonded together by adhesive materials, and they play a major role in determining the strength of the whole assembly for aerospace, automobile, fashion industry, and many other manufacturing sectors. Peeling tests are routinely performed to assess the quality of bonding and determine the adhesive properties requested to withstand applied loading. The peeling test gives in output the peeling force required to delaminate a deformable layer/film from the substrate. As compared to a fully bonded interface where the continuity of tractions and displacements is guaranteed at the material discontinuity, the response of an adhesive interface evolves during debonding, with a progressive separation and tractions that are nonlinearly function of the displacement discontinuities [1, 2].The expression of the traction-separation law (TSL) relation is usually called cohesive zone model (CZM), see [3, 4, 5, 6] for some relevant examples and functional relations.

Analytical solutions for peeling tests addressing the mixed-mode deformation problems have been notably derived in [7, 8, 9]. Other relevant contributions towards the understanding of the mechanics and failure of cohesive interfaces in statics and dynamics, among the many published in the literature, are those in [10, 11, 12, 13, 14, 15, 16]. In terms of computational methods, the CZM for adhesive interfaces can be efficiently implemented within the finite element method (FEM) according to an intrinsic approach, duplicating the nodes of finite elements sharing an interface and inserting zero-thickness interface finite elements along the adhesive interface [17]. In case of non-conforming meshes, node-to-segment interface elements derived from contact mechanics can be exploited as well, as shown in [17]. The method is robust in handling non-linear problems using a full-implicit Newton-Raphson incremental-iterative

scheme. In some engineering applications, CZM is also combined with Extended Finite Element Method (XFEM) or with the phase field modeling (PFM) technique [18, 19, 20, 21, 22] that provide a comprehensive and accurate representation of crack initiation, delamination, propagation, and interaction with microstructural features.

In the present work, the exponential CZM formulation in [5] is adopted to describe the nonlinear response of an adhesive joining a bi-material system which may undergo delamination. Instead of setting all the parameters of the CZM, which are the peak tractions in Mode I and Mode II, and the critical normal and tangential gaps for complete decohesion (or, analogously, the Mode I and the Mode II fracture energies which are functions of the above parameters), we herein explore the possibility to identify optimal properties of the interface to preserve the response of the composite even in presence of evolving debonded regions. Specifically, the possibility of a functionally graded interface with a linear variation of fracture energy along the interface coordinate is explored, motivated by the fact that such kind of interfaces could be technologically manufactured by acting on their microstructure, for instance by varying the geometry and/or the density of mushroom micro-pillars in Gecko's bio-inspired adhesives [23, 24, 25, 26, 27, 28, 29]. The main objective is to assess the potential of such functionally graded interfaces in withstanding debonding, to make the composite material delamination-tolerant.

Therefore, the material parameter identification of the CZM parameters becomes an inverse problem. To solve it, non-gradient-based algorithms which can be included within a category of *data-driven* approaches are genetic algorithms [30], particle swarm optimization [31], Cuckoo search algorithm [32], evolutionary algorithms [33], to name a few. In the literature, data-driven machine learning models [34, 35, 36, 37] have been employed to gain insights into the traction-separation relationship and the underlying physics of interface problems. Several researchers [38, 39, 40, 41] worked on non-gradient optimization models for inverse parameter identification of CZM interface properties. Optimization methods play a crucial role in accurately determining the CZM parameters. In this direction, the fracture mechanics field is experiencing significant transformation due to advancements in machine learning, data-driven methods, and modern computing tools. These models are essential for predicting material fracture behavior with greater reliability. By utilizing different optimization algorithms and rigorously validating the results, researchers can improve the fidelity and practical applicability of CZMs in engineering applications. In the present study, the particle swarm optimization (PSO) algorithm will be employed since it overcomes local minima issues compared to the above-mentioned optimization models, and it has already been proven to be efficient for non-convex strongly nonlinear problems in the context of plasticity and cohesive fracture [42] and for material identification problems in phase field fracture [43]. In conclusion, *data-driven* modeling offers substantial promise in various areas, including identifying physical parameters and discovering new physics when creating new materials.

The second objective of the work is to assess the possibility to make a bi-material

component with an imperfect adhesive interface tolerant to interfacial defects by acting on the optimization of the topology of the surrounding continuum. Topology optimization is carried out for this class of inverse problems based on physics-based simulated data. Relevant publications on topology optimization (TO) used in simpler contexts without fracture are available in [44, 45, 46, 47]. The technique is usually applied to design lightweight structures preserving the mechanical response [48]. Since then, several topology optimization techniques, including density-based [49], level-set method [50], Evolutionary Structural Optimization (ESO) [51], Bi-directional Evolutionary Structural Optimization (BESO) [52], and others have been proposed in the literature. Those methods exploit optimization techniques to distribute the material inside the design space with a design variable which can take dichotomic values (1 for the solid, 0 for the empty region), or with a continuous variation in that range. The level set method, ESO, and BESO optimization approaches use the discrete design variable approach. The continuous technique uses a solid isotropic material with penalization (SIMP) approach. It is specifically utilized in density-based optimization, where the method of moving asymptotes (MMA) [53] and the Optimality Criteria (OC) [54] are employed to solve the topology evolution of structural problems within the design constraints. The Optimality Criteria (OC) method is more widely used than the Method of Moving Asymptotes (MMA) because it has a more straightforward explanation and implementation. OC involves updating design variables based on analytical expressions derived from optimality conditions, making it computationally efficient and often faster for compliance minimization problems. The MMA is more complex to implement but is recommended for nonlinear topology optimization problems that involve multiple loading conditions, constraints, and objectives. However, since our current work does not involve such complexities, the OC method is herein selected. In recent research, TO has been effectively applied to enhance the toughness of heterogeneous adhesive films [55] by strategically arranging stiff and soft material blocks, or exploring functionally graded materials in the context of phase-field fracture [56].

In the present work, we seek topology optimization of the substrate corresponding to a certain portion of the deformable layer peeled off. The interface response is again described by a linearly graded CZM, as analyzed in Sec.2. The substrate stiffness is considered as an objective function with volume constraints. The sensitivity analysis of the objective function with respect to the design variable is carried out, and the OC method is applied to evolve the design variable with design iterations until the user-defined condition is met. Finally, the optimized substrate topology is determined. The evolution of the optimal substrate topology patterns for different volume fractions is analyzed, and different amounts of interface delamination are also investigated to assess the robustness of the identified topology under perturbations in the extent of the onset of delamination.

The article work is organized as follows: the mathematical framework for the cohesive zone modeling (CZM) for a graded interface is outlined in Sec.2. Sec.3 ad-

dresses the problem of identification of optimal properties of linearly graded cohesive interface by exploiting the PSO algorithm. Sec.4 discusses how to find the optimal structural topology of a substrate under the influence of imperfect adhesive bonding, by exploiting the SIMP gradient-based optimization algorithm. Finally, the article conclusions are provided in Sec.5.

2. Graded cohesive zone interface model

The current work assumes the structure behavior obeys small strain deformation theory. As shown in Fig.1, we consider a continuum domain Ω in which a deformable substrate B1 and a second material B2 are connected by an adhesive which mathematically provides continuity of tractions at the interface and an evolving separation in the normal and in the tangential directions (defined in local reference system). By the principle of virtual work, which leads to the weak form of the mechanical system, the total energy including the contribution of cohesive tractions at the interface reads:

$$\delta\Pi = \int_{\Omega} \sigma \, \delta\boldsymbol{\varepsilon} \, \mathrm{d}\Omega - \int_{\Omega} \mathbf{b} \, \delta\mathbf{u} \, \mathrm{d}\Omega - \int_{\partial\Omega_t} \delta\mathbf{u} \, \mathrm{d}\partial\Omega_t - \int_{\partial\Omega_s} \mathbf{t}_{\mathrm{coh}} \, \delta\Delta\mathbf{u} \, \mathrm{d}\partial\Omega_s \tag{1}$$

where σ represents the Cauchy stress tensor, $\delta\boldsymbol{\varepsilon}$ denotes the virtual variation of the strain field associated to the displacement field $\mathbf{u}$, $\mathbf{b}$ and $\bar{\mathbf{t}}$ represent the body forces and the imposed boundary tractions acting on Ω and $\partial\Omega_t$, respectively. The vector of cohesive tractions is $\mathbf{t}_{\mathrm{coh}}$, which contributes to the virtual work through the associated virtual variation of the relative displacement vector $\delta\Delta\mathbf{u}$ along the interface $\partial\Omega_s$.

The finite element formulation associated to the cohesive interface model used in the present work is based on the 4-node zero thickness interface finite element whose matrix expression and algorithmic implementation as a user element can be found in [17] and are omitted here for the sake of brevity. The formulation implemented in [17] within the research finite element software FEAP [57] has been re-implemented here in a user element for the open source finite element research code DAEdalon [58] based on MATLAB R2022, which facilitates the interaction between FEA and optimization algorithms, without the need of introducing input/output software interfaces.

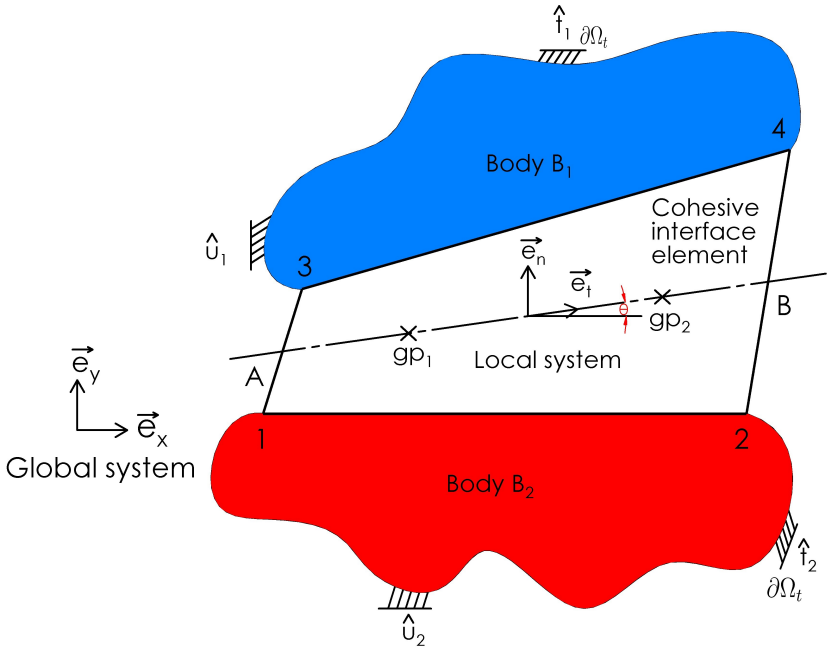

fig. 1. Schematic representation of a zero thickness interface element.

Due to the external load applied to the structure, the cohesive interface region can delaminate and this phenomenon is governed by a Mixed Mode traction-separation relation. Here, for its versatility, we consider the version proposed by Tvergaard [5], although any other functional relations could be analogously exploited, without any loss of generality. The σ_n and τ_t cohesive tractions composing the vector $\mathbf{t}_{\text{coh}}$ are nonlinear functions of the normal and tangential gaps g_n and g_t:

$$\begin{aligned} \sigma_n &= \sigma_{\max} \frac{g_n}{g_{n_c}} f(\beta) \\ \tau_t &= \tau_{\max} \frac{g_t}{g_{t_c}} f(\beta) \end{aligned} \tag{2}$$

where g_{n_c} and g_{t_c} are the critical normal and tangential gaps for complete decohesion under pure Mode I or Mode II deformation, $f(\beta)$ is a function which establishes a measure of mode mixity, and $\sigma_{\max}$, $\tau_{\max}$ are the maximum normal and tangential tractions that the interface can withstand, respectively, in pure Mode I or Mode II deformation. For the Tvergaard CZM we have:

$$\beta = \sqrt{\left(\frac{g_n}{g_{n_c}}\right)^2 + \left(\frac{g_t}{g_{t_c}}\right)^2} \tag{3}$$

and

$$f(\beta) = \begin{cases} \frac{27}{4}\left(1 - 2\beta + \beta^2\right), & \text{for } 0 \leq \beta \leq 1 \\ 0, & \text{otherwise} \end{cases} \tag{4}$$

The CZM relation is graphically shown in a qualitative manner in Fig.2 in terms of $t_{\rm coh}$ vs. g_n and g_t. Under pure Mode I conditions, the area below the $t_{\rm coh}$ vs. g_n curve for $g_t = 0$ leads to the Mode I fracture energy $\rm G_{IC}$. Similarly, the area below the $t_{\rm coh}$ vs. g_t curve for $g_n = 0$ leads to the Mode II fracture energy $\rm G_{IIC}$. Here, we shall consider two functional forms for the CZM relation: (i) homogeneous properties throughout the interface (ii) linearly graded fracture toughnesses.

In both cases, maximum tractions are the same, while the graded interface model introduces a linear dependency of the critical normal and tangential displacements upon the interface coordinate x defined in the global reference frame, see Fig.3.

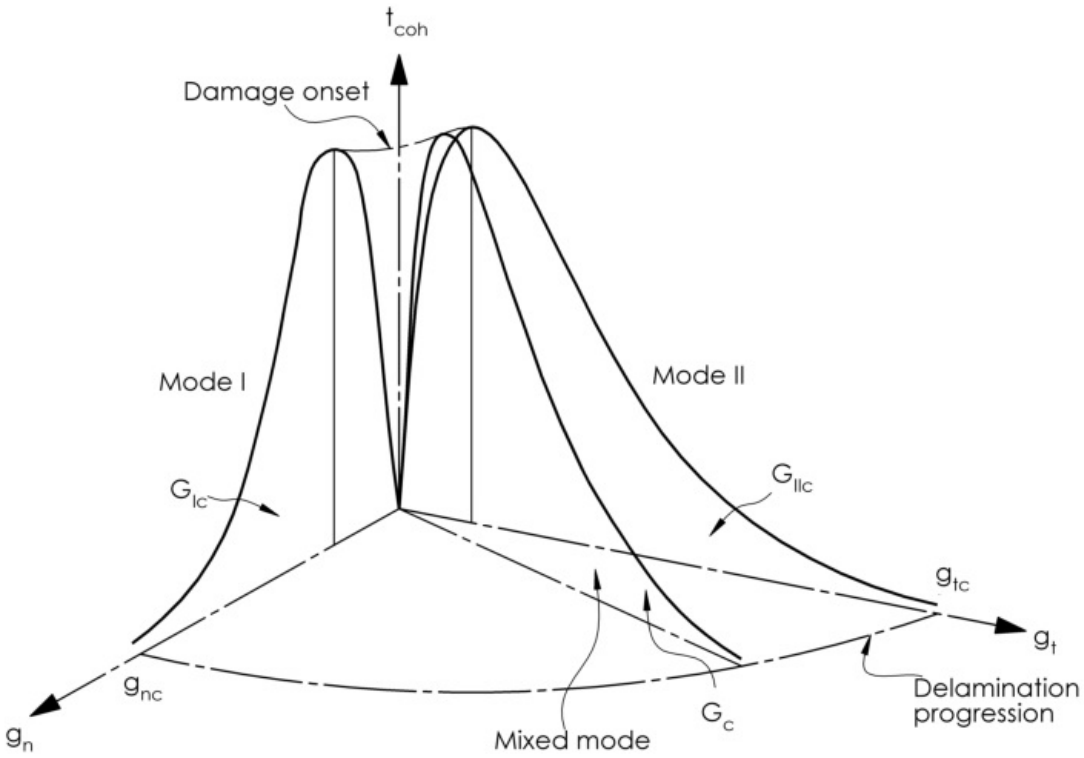

fig. 2. Tvergaard exponential law cohesive zone model

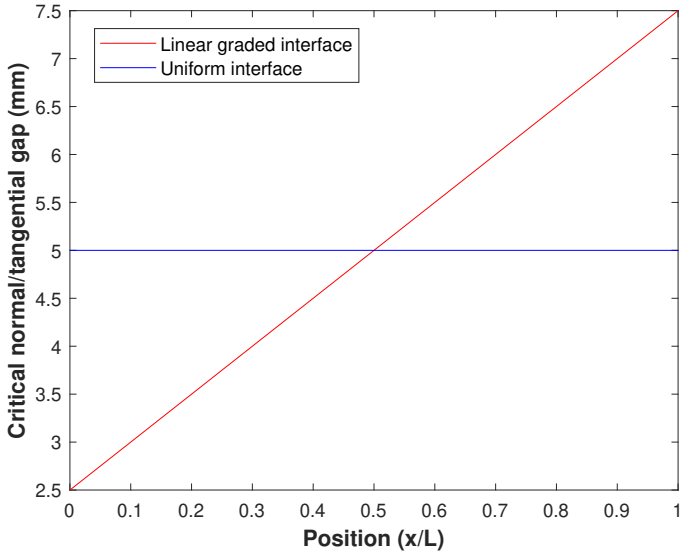

fig. 3. Linear graded interface model: critical cohesive normal and tangential gaps, g_{n_c} and g_{t_c} for complete decohesion vs. interface position x/L, where L denoted the maximum extension of the interface. The curve in black shows the value of the parameters for an interface with uniform properties averaged over the interface length.

3. Optimum functional grading properties of cohesive interfaces

In this section, we analyze the failure of linearly graded interfaces and we compare their performance with that of an interface with uniform averaged properties. Then, we show how to apply a data-driven machine learning technique to automatically find the properties of the linearly graded interface to maximize the functional performance of a structure subject to delamination.

3.1. Analysis of a linearly graded cohesive interface

The 2D numerical model of the peeling test that will be used as benchmark for the analyses is shown in Fig.4. The deformable layer with a height of 0.05 mm is peeled off from a stiffer substrate which is 1 mm deep. The lateral size of the whole numerical model is $L = 1$ mm. The progress of separation till failure of the interface is governed by the traction-separation (TS) law.

The Youngs' modulus of the deformable layer is set equal to 2.8 GPa, and that of the substrate 73 GPa, which is a physical scenario for a thin deformable layer bonded onto an almost rigid substrate. For what concerns the boundary conditions, Fig.4, the bottom left corner node is constrained in the horizontal and vertical direction while the remaining nodes at the bottom edge are constrained on the vertical direction. For the deformable layer, horizontal displacements at the nodes belonging to the edge on the left are constrained.

Contact constraints were incorporated into the CZM using the penalty method active in compression with a stiffness $k_p = 1000$ N/mm^2 to avoid the compenetration of materials along the interface. The linearly graded interface properties for the Tvergaard CZM are: $\sigma_{\max} = \tau_{\max} = 20$ MPa, $g_{n_c} = g_{t_c} \in (2.5 - 7.5)$ mm. Hence, the critical normal and tangential gaps vary linearly from 2.5 mm at $x = 0$ to 7.5 mm at $x = L$, as shown in Fig.3. For this benchmark problem, the Mode I and Mode II TSL properties are the same.

FEM simulations are conducted under plane strain assumptions. The peeling test problem has been discretized with 4-noded isoparametric quadrilateral elements. The substrate has been discretized with 100×4 elements, since it is almost rigid. The interface region has been discretized with 100 elements along its length, while the deformable layer has been discretized with 100 elements along its length and 6 over its thickness, to capture its bending deformation.

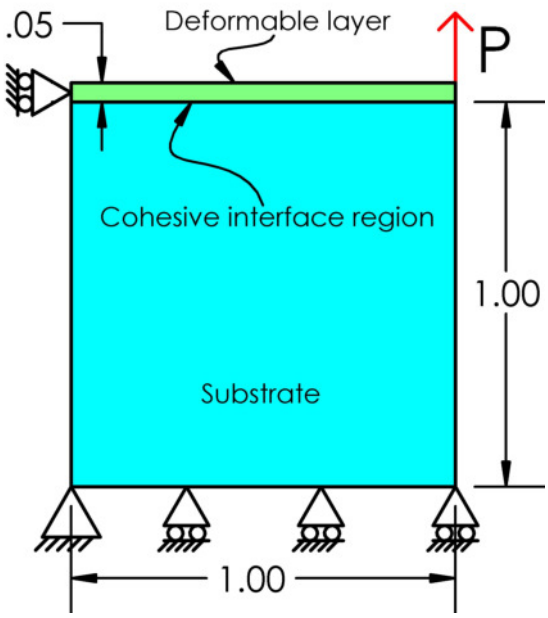

fig. 4. Model sketch of the peeling test.

The top right corner of the deformable layer is subject to a prescribed displacement as external loading. The corresponding force P is computed as a reaction force in the node. For the model test problem chosen, the mentioned loading leads to Mixed-Mode delamination. The evolution of the reaction force P for an interface with uniform properties and for a linearly graded one are shown versus the imposed displacement in Fig.5, with a typical trend as reported in the literature [11, 59, 12]. The linearly graded interface, although in average has the same properties of the uniform one, has a spatial distribution of its fracture toughness which is highly beneficial, since it offers a stronger opposition to the onset of debonding through its higher value of G_C at $x = L$. As a consequence, the peak force for the onset of debonding is enhanced.

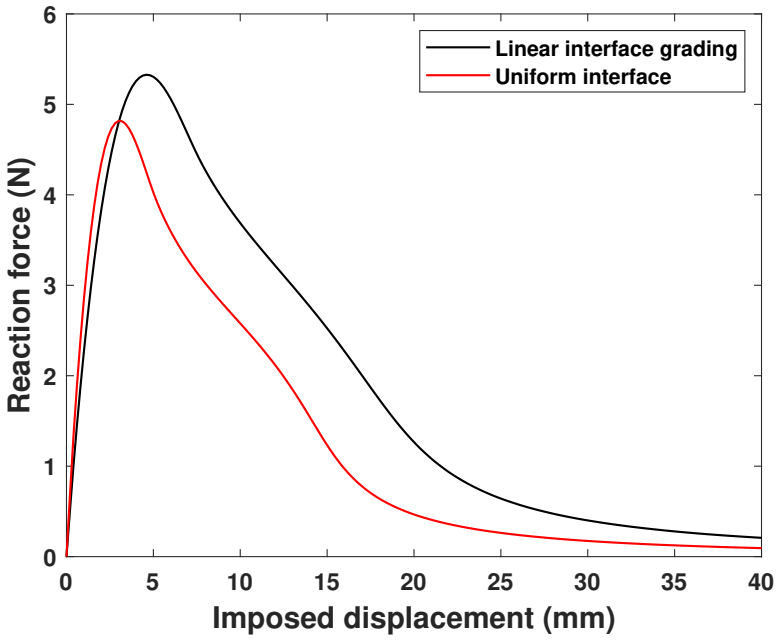

fig. 5. Reaction force P versus imposed displacement for a linearly graded interface in comparison to an interface with uniform properties.

Looking into more details on what happens along the interface in the two scenarios, we notice that the interface with graded properties generates a non-uniform normal traction at the interface which is quite different as compared to the uniform case, see Fig.6. Normal traction curves vs. x/L superimposed to those figures correspond to an increasing applied displacement (moving from the curve in red to the one in light black). The graded interface allows delaying the onset for delamination as compared to the interface with uniform properties, see the red curve at $x/L = 1$ that, for the uniform one, is already approaching zero while for the graded interface has a residual value of about 10 MPa, i.e., it is still partially bonded.

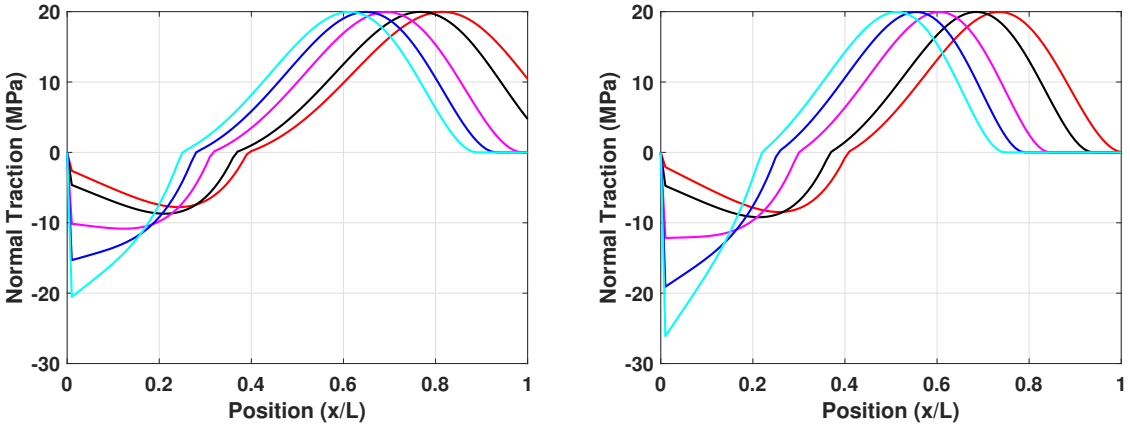

(a) Linear graded cohesive interface **(b)** Uniform cohesive interface

fig. 6. Comparison of normal tractions vs. position for a linearly graded interface and an interface with uniform interface properties for different far-field prescribed displacements increasing in the curves from red to light black.

3.2. Machine learning identification of graded interface properties

The benchmark test in Sec.3.1 motivates the development of a machine learning technique that can automatically identify the properties of a linearly graded cohesive interface to achieve a desired (target) mechanical response. For those problems, the target response can be the maximum reaction force measured during the peeling test, or even a measure of the error in a suitable norm between the predicted force-displacement curve and the experimental one to be identified.

For what concerns the candidate algorithms, there are numerous nature-inspired [31, 30, 32], evolutionary [60] and population [61] based algorithms available in the literature. In the present work, particle swarm optimization (PSO), a machine learning algorithm best suited for data-driven inverse problems [42, 43], is exploited to identify the interface properties. PSO [31] is a nature-inspired algorithm that looks for the best answer inside the solution space. It does not rely on the gradient of the objective function, whose functional expression is unknown, while it requires the sampling of the objective function in the hyper-parameter space, so it can be considered as a data-driven approach.

The method is based on a certain number of swarm particles dispersed in the solution space, and we seek to converge to a solution which is minimizing the cost function $\mathscr{Z}$. The model test problem (see Fig.4) with linearly graded interface properties is herein examined. The cost function to be minimized is herein defined as the error in the L2 norm between the predicted and the desired reaction force-displacement curve:

$$\mathscr{Z}(\chi) = 1 - \frac{1}{N}\sum_{d=1}^{N}\sqrt{\left[\frac{\Delta Rx_d(\chi)}{\hat{R}x_{\max}(\chi)}\right]^2} \tag{5}$$

where $\Delta Rx_d(\chi) = Rx_s - Rx_t(\chi)$. Rx_s denotes the history of simulated reaction forces for the range of imposed pseudo-time steps d ($d = 1, \ldots, N$). The model test problem is conducted under displacement control till the N values of applied displacement are imposed, for a given set of PSO model parameters. Analogously, $Rx_t(\chi)$ represents the target value of the reaction forces for the same values of the N imposed displacements. $\hat{Rx}_{\max}(\chi) = \max(\max(Rx_s), \max(Rx_t(\chi)))$ denotes the maximum value of the reaction force out of the $Rx_s, Rx_t(\chi)$ values considering N imposed displacements. The cost function would tend to $\mathscr{Z}(\chi) = 1$ if the PSO simulated curve and the target response are the same. The properties chosen to numerically generate the target response for a linear graded interface are $\sigma_{\max} = \tau_{\max} = 20$ MPa, $g_{n_c} = g_{t_c} \in (2.5 - 7.5)$ mm.

For the inverse parameter identification problem, three properties are considered as free parameters: the maximum normal traction, $\sigma_{\max}$, the critical normal gap $(g_{n_c})_L$ for the interface at $x = L$, and the critical normal gap $(g_{n_c})_0$ at $x = 0$. The Mode II model parameters: the maximum shear traction, $\tau_{\max}$, the critical tangential gaps $(g_{t_c})_L$, $(g_{t_c})_0$ for the interface at $x = L$, $x = 0$ respectively are set the same as Mode I model parameters during analysis and therefore are not included in the parametric space.

The feasibility domain is defined sufficiently wide to explore all the physical solutions of the problem that are of potential interest:

$$\Upsilon = \{10 < \sigma_n < 30 \text{ MPa}; 0.01 < (g_{n_c})_0 < 4 \text{ mm}; 5 < (g_{n_c})_L < 10 \text{ mm}\} \tag{6}$$

In the PSO algorithm, the swarm particles are composed of particle position and velocity vector. The particle position vector at the k-th iteration is given as

$$\chi_{\mathbf{i}}^{\mathbf{k}} = \chi_{\mathbf{i}}^{\mathbf{k-1}} + \bigvee_i^{\mathbf{k}} \tag{7}$$

where $\bigvee_i^{\mathbf{k}}$ is the velocity vector of the constriction factor-based approach [62] given by Eq.(8):

$$\begin{aligned} \bigvee_i^{\mathbf{k}} &= \kappa \times (\bigvee_i^{\mathbf{k-1}} + \mathbf{C_c} \times \mathbf{r_1} \times (\mathbf{P_i^k} - \chi_{\mathbf{i}}^{\mathbf{k}}) + \mathbf{S_c} \times \mathbf{r_2} \times (\mathbf{P_g^k} - \chi_{\mathbf{i}}^{\mathbf{k}})) \\ \kappa &= \frac{2}{\left|2 - \varphi - \sqrt{\varphi^2 - 4\varphi}\right|}, \text{where } \varphi = \mathbf{C_c} + \mathbf{S_c}, \varphi > 4 \end{aligned} \tag{8}$$

being κ a constriction factor and $\mathbf{r_1}, \mathbf{r_2}$ are random numbers between 0 and 1. To guarantee stability [63], φ was set as 4.1 and $\mathbf{C_c} = \mathbf{S_c} = 2.05$, where $\mathbf{C_c}, \mathbf{S_c}$ represent, respectively, the cognitive coefficient and the social coefficient, whose terminology comes from applications of PSO to problems in behavioral economics. $\mathbf{P_i^k}$ is the best solution for the particle i until iteration k, and $\mathbf{P_g^k}$ is the best solution computed among all the swarm particles.

The application of PSO to the present problem leads to the evolution of swarm particles' position within the design solution space shown in Fig.8. The identified

interface fracture properties at the end were $\sigma_{max} = 20.0001$ MPa, $(g_{n_c})_0 = 2.5221$ mm, and $(g_{n_c})_L = 7.5$ mm, which are very close to the values used to generate the target curve.

The evolution of the cost function is depicted in Fig.7(a), and the comparison between the identified response and the target response at convergence is shown in Fig.7(b).

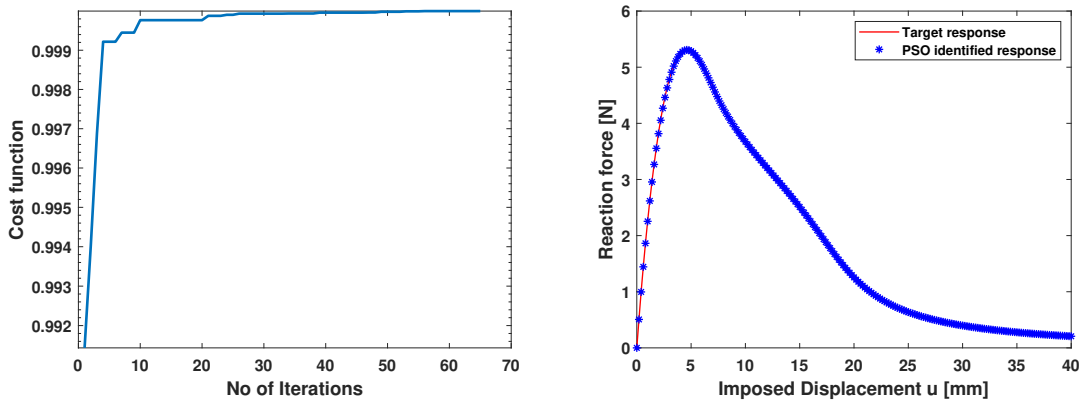

(a) Cost function **(b)** Identified response at convergence

fig. 7. (a) Cost function vs. number of PSO iterations; (b) comparison between PSO identified response and target response at convergence for the peeling test problem with a linearly graded interface.

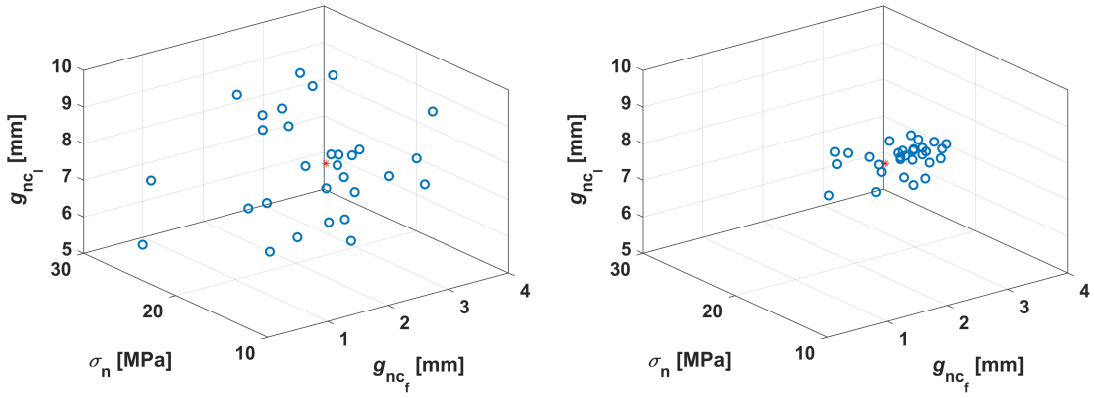

(a) Initial particles' position

(b) Iteration No. 4

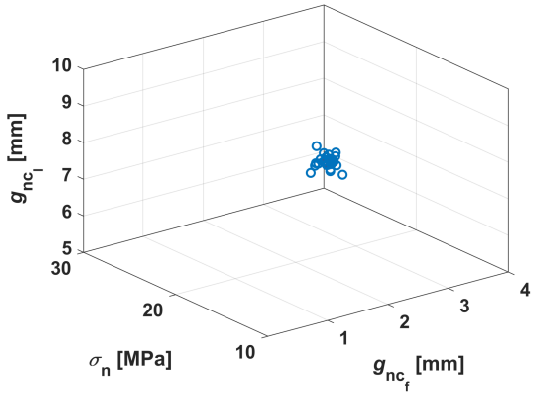

(c) Iteration No. 15

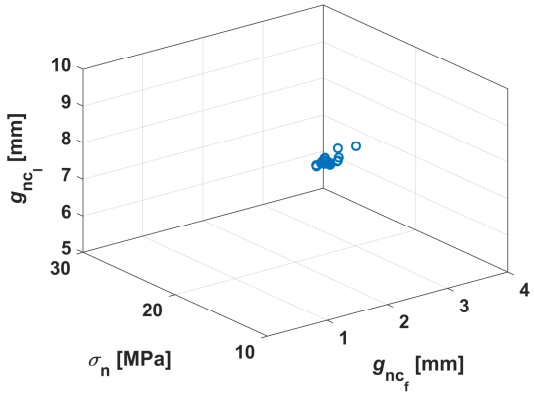

(d) Iteration No. 30

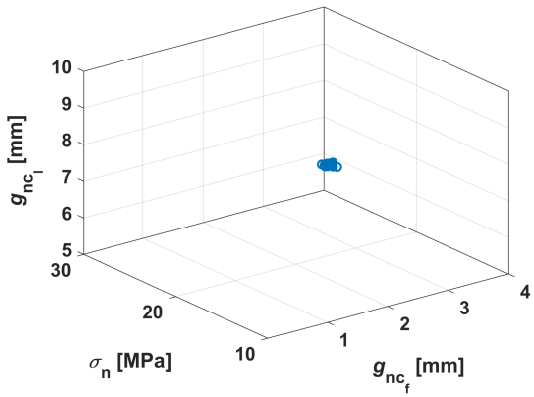

(e) Iteration No. 45

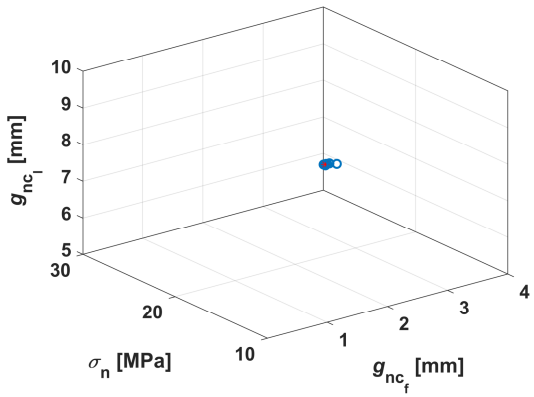

(f) Iteration No. 65

fig. 8. Position of the particles during the progress of the iterations of the PSO algorithm applied to the peeling test problem with a linearly graded interface.

4. Topology optimization of substrates prone to delamination

In this section we deal with structural design topology optimization problems under the influence of cohesive interface fracture. Before that, an initial background of topology optimization and a few benchmark problems will be discussed.

4.1. Topology optimization implementation

The algorithm for topology optimization proposed in [54] is examined in the present work. The design domain, denoted as Ω, is discretized into N_e finite elements, and each element e is assigned a topology density variable ϕ_e. The solid isotropic with penalization (SIMP) material interpolation [64] is incorporated in the design domain, which is controlled by the continuous design density variable ϕ_e. The design variable ϕ_e ranges between $0-1$, which varies within the discrete element of the structure, being 0 a void material and 1 a solid material. Hence, the material is interpolated as follows:

$$E\left(\phi_e\right) = E_{\min} + \phi_e^p \left(E_0 - E_{\min}\right), \quad \phi_e \in [0,1] \tag{9}$$

where $E\left(\phi_e\right)$ denotes the Young's modulus of the e-th element, $E_{\min}$ is a dummy Young's modulus much smaller than the other ones to model a void (here we set it equal to 10^{-9}). E_0 is the Young's modulus of the material whose structural topology has to be optimized, p is a penalty coefficient and in the literature a value of 3 [65] is typically chosen to ensure a clear distinction between a solid and a void.

The mathematical formulation of the current topology optimization problem reads as follows:

$$\begin{aligned} &\text{Minimize: } C(\phi) = \mathbf{U}^{\mathrm{T}}\mathbf{K}\mathbf{U} = \sum_{e=1}^{N} E_e\left(\phi_e\right)\mathbf{u}_e^{\mathrm{T}}\mathbf{k}_0\mathbf{u}_e \\ &\text{subject to : } \mathbf{K}\mathbf{U} = \mathbf{F} \\ &\sum_{e=1}^{N_e} \phi_e v_e \Big/ \left(\sum_{e=1}^{N_e} v_e\right) = f \\ &0 \le \phi_e \le 1; \quad e = 1, 2, \ldots, N_e \end{aligned} \tag{10}$$

where $C(\phi)$ is the objective function that depends on the design variable ϕ, and it is proportional to the internal work of the mechanical system. Here, v_e represents the e-th elemental volume in the design domain, such that the material distribution has to comply with the prescribed volume fraction f. $\mathbf{K}$,$\mathbf{U}$, and $\mathbf{F}$ denote, respectively, the assembled global stiffness vector, the displacement vector, and the load vector.

The optimization problem in Eq.(10) can be solved by means of optimality criteria method [54, 66] based on the following heuristic updating scheme:

$$\phi_e^{\text{new}} = \begin{cases} \max\left(0, \phi_e - m\right) & \text{if } \phi_e B_e^{\eta} \le \max\left(0, \phi_e - m\right) \\ \min\left(1, \phi_e + m\right) & \text{if } \phi_e B_e^{\eta} \ge \min\left(1, \phi_e - m\right) \\ \phi_e B_e^{\eta} & \text{otherwise} \end{cases} \tag{11}$$

where m is a positive moving limit, $\eta = 1/2$ is a numerical damping coefficient, and B_e is obtained from the KKT optimality condition given below:

$$B_e = -\frac{\partial c(\phi)}{\partial \phi_e}\left(\lambda \frac{\partial v(\phi)}{\partial \phi_e}\right)^{-1} \tag{12}$$

where λ is a Lagrangian multiplier chosen to satisfy the volume constraint and its appropriate value can be found by employing a bisection algorithm. Moreover, the sensitivities of the objective function $c(\phi)$ and the material volume v concerning the element densities ϕ_e are computed as:

$$\begin{aligned} \frac{\partial c(\phi)}{\partial \phi_e} &= -p\phi_e^{p-1}\left(E_0 - E_{\min}\right)\mathbf{u}_e^{\mathrm{T}}\mathbf{k}_0\mathbf{u}, \\ \frac{\partial v(\phi)}{\partial \phi_e} &= 1. \end{aligned} \tag{13}$$

To ensure the existence of solutions to the topology optimization problem and to avoid the formation of checkerboard patterns [67, 68] the sensitivity filtering technique [65] is introduced as follows:

$$\tilde{\rho}_e = \frac{\sum_{j\in N_e} W_{e,j}\phi_j \dfrac{\partial c(\phi)}{\partial \phi_j}}{\max(\alpha, \phi_e)\sum_{j\in N_e} W_{e,j}} \tag{14}$$

where

$$W_{e,j} = \begin{cases} \frac{R_0 - r_{ej}}{R_0} & \text{for } r_{ej} < R_0 \\ 0 & \text{for } r_{ej} \geq R_0 \end{cases} \tag{15}$$

being $\tilde{\rho}_e$ the sensitivity filter which modifies the sensitivities of the objective function $c(\phi)$ in Eq.(13); N_e is the subset containing the surrounding elements within the filtered radius R_0 to the e-th element; α in Eq.(14) is set equal to 10^{-3} to avoid division by zero. $W_{e,j}$ is the linearly decaying cone shape weighted filtering function of elements e and j, ϕ_j is the non-filtered density of the j-th element within the filtered radius R_0, r_{ej} is the distance between the center of the element e to that of the element j.

4.2. Numerical examples

The above algorithm is applied to a series of benchmark problems without the issue of delamination to identify a structural topology that is able to maximizing its stiffness (or, viceversa, minimize its compliance). The results of the optimum topology of the benchmark problems with also details on the portion of the material withstanding tensile (in red) or compressive (in black) stress states is provided in the Appendix.

Now, the methodology is challenged here in relation to the problem geometry already investigated in the previous section, where a thin layer is peeled off from

the substrate; see the sketch in Fig.9. In this problem, the interface region has been discretized with 75 elements along its length, while the deformable layer has been discretized with 75 elements along its length and 8 over its thickness, and the optimization region (substrate) is discretized with 75 $\times$ 75 elements. The top right corner of the deformable layer has a prescribed displacement imposed, that leads to a reaction force P during the evolution of delamination.

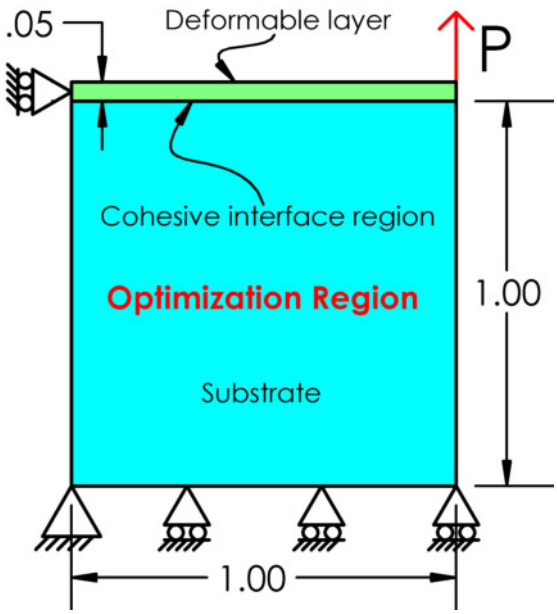

fig. 9. Sketch of peeling test with boundary conditions for a substrate with a delaminating interface, where the topology of the substrate has to be optimized to maximize the stiffness of the mechanical system for different levels of delamination.

The substrate region is the focus of our study concerning topology optimization. Linearly graded cohesive interfacial properties are set equal to $\sigma_{\max} = \tau_{\max} = 10$ MPa, $g_{n_c} = g_{t_c} \in (2.5 - 7.5)$ mm, where the critical normal and tangential gaps vary both linearly from 2.5 mm at $x = 0$, up to 7.5 mm at $x = L$.

Considering a displacement load that increases linearly over a pseudo-time variable, we can simulate stress conditions in the substrate corresponding to varying degrees of progressive delamination of the bonded layer, focusing on scenarios typical of the onset of debonding. The topology optimization algorithm is applied after a specific portion of the interface layer has debonded, and the structural topology evolution of the substrate is studied. Further results investigate the influence of the substrate volume fraction on optimum topology and compliance values, followed by a study on topology optimization of the substrate subject to different prescribed displacement loading conditions, which in the present case correspond to different portions of initial interface delamination.

4.3. Impact of volume fraction

The optimum topology of the substrate was initially studied for different volume fractions under identical loading conditions. For this analysis, five different substrate volume fractions $f = 10\%$, 20%, 30%, 40%, and 50% were examined. The numerical topology optimization process, as outlined in Fig.11, was applied. Initially, a total displacement of 9 mm was imposed at the top-right corner node, resulting in delamination up to 0.08 mm along the interface. Subsequently, the topology optimization (TO) process was conducted for various substrate volume fractions. The findings indicate that the volume fractions $f = 10\%$ and 20% did not yield practically feasible designs and exhibited very high oscillations in compliance value throughout the iterations. However, volume fractions $f = 40\%$ and 50% are promising for achieving feasible optimized topological designs as depicted in Fig.13 (b),(c). In the figures, red color represents the solid material, while black indicates void. Interestingly, the topology pattern remains consistent for $f = 30\%$, 40% and 50% volume fraction-optimized structures. The impact of volume fraction f on the mean compliance for $f = 30\%$, 40% and 50% is shown in Fig.12, which shows a decrease in the mean compliance with an increase in volume fraction f. A comparison of the compliance value with respect to the number of design iterations for volume fractions $f = 30\%$, 40% and 50% is shown in Fig.13, revealing that the optimized substrate with $f = 50\%$ is stiffer than those with $f = 30\%$ and 40%, as more material volume is available to resist delamination. This study provides valuable insights into evaluating the best-optimized designs for interface problems while considering cost implications without compromising the system's performance. This analysis is highly beneficial for industrial applications focused on finding optimized structures, especially when design constraints are clearly defined, to ensure better functionality of the structure.

4.4. Discussion on different far-field imposed displacements

We examined two cases to study the topology evolution of the substrate under different far-field imposed displacements. The volume fraction f of the substrate is set to 0.5, which provides better structural strength out of $f = 30\%$, 40% and 50% as mentioned in Sec.4.3. In the first case, a total displacement of 9 mm is applied to the top right corner node, resulting in delamination of up to 0.08 mm along the interface. With the displacement load fixed, the topology optimization algorithm is iteratively applied. The detailed algorithmic implementation of FEM-TO is illustrated in Fig.11. The resulting structural topology evolution of the substrate is shown in Fig.14. In the second case, a total displacement load of 12 mm is applied, leading to a longer delamination of 0.2133 mm along the interface. The structural topology evolution of the substrate was recomputed and is displayed in Fig.15. The different far-field total imposed displacements in cases 1 and 2 cause the non-linear response of the linearly graded cohesive interface properties to generate different stress fields and compliance values. Consequently, different optimized structural topology patterns emerge, as seen in Figs.14 and 15 for the two test problems. Despite some local variations, the patterns are quite similar, suggesting that it is effective to design substrate topologies

with localized densities to maximize the structure's stiffness and resist delamination events.

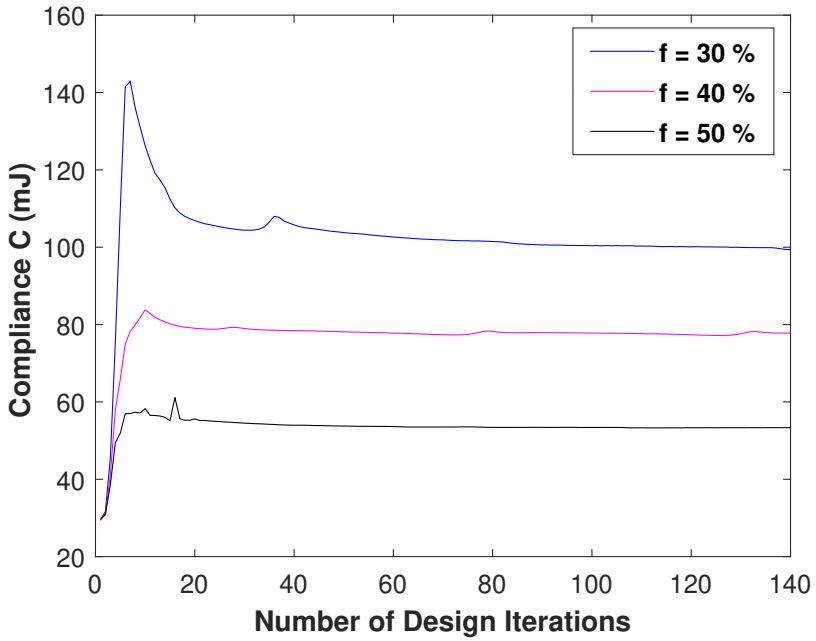

fig. 10. Comparison of compliance value with respect to number of design iterations for different volume fractions f.

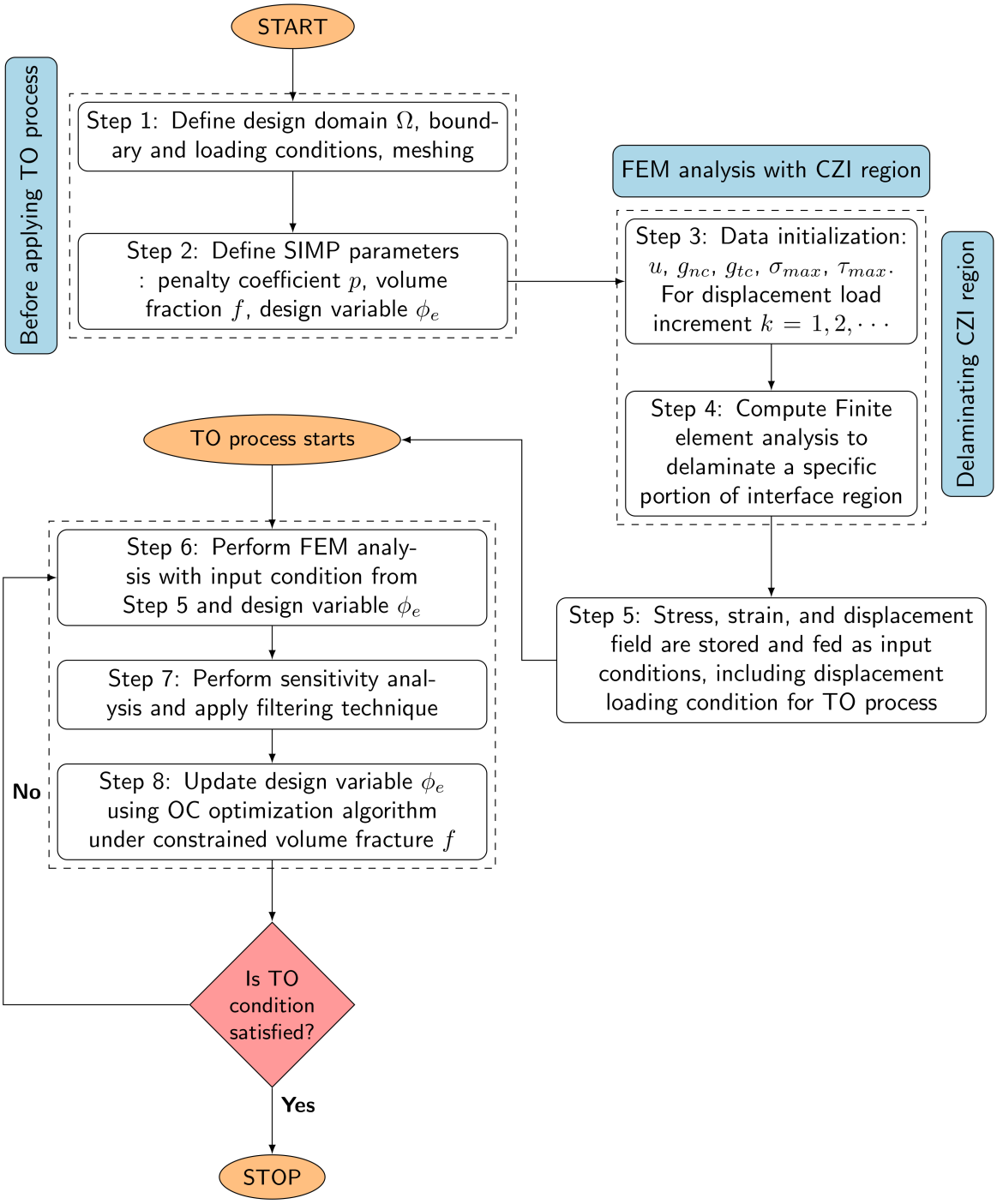

fig. 11. Flow chart showing combined FEM-TO algorithm for topology optimization of substrate in correspondence of different portions of initial delamination along the interface.

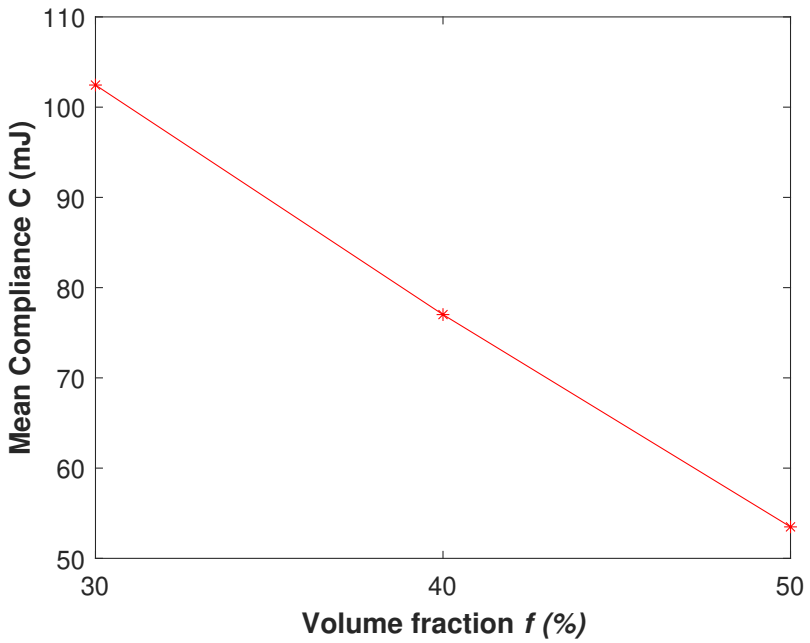

fig. 12. Trend showing mean compliance (C) as a function of volume fraction (f)

(a) $f = 30\%$ **(b)** $f = 40\%$ **(c)** $f = 50\%$

fig. 13. Optimized substrate topology for different volume fractions.

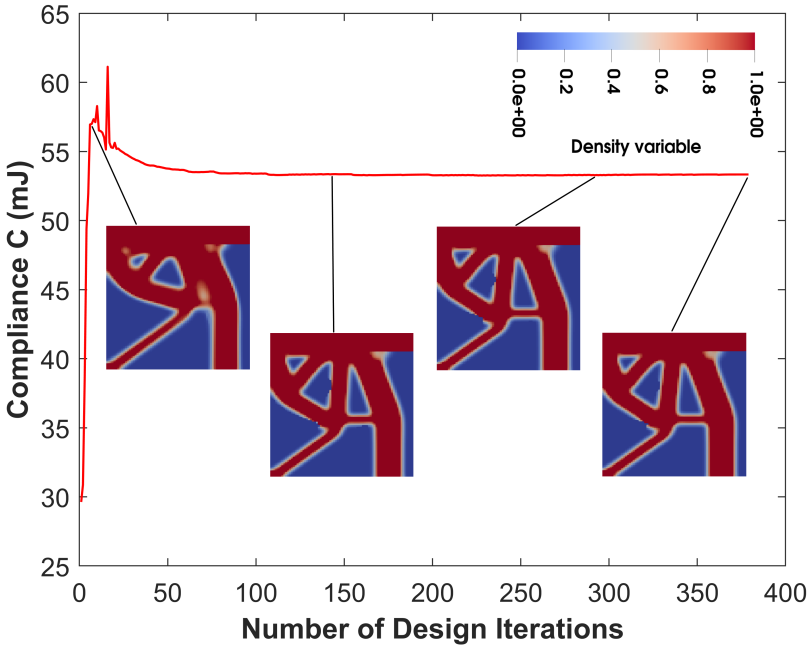

fig. 14. Structural topology evolution of the substrate for an interface with initial debonding of 0.08 mm.

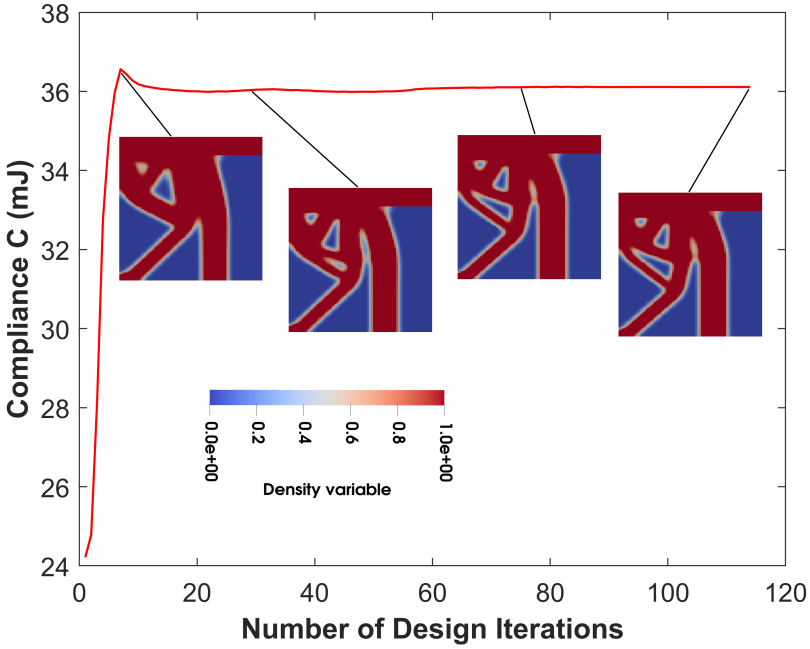

fig. 15. Structural topology evolution of the substrate for an interface with initial debonding of 0.2133 mm.

The current topology optimization framework has been extended to investigate L-shaped structural geometry similar to as mentioned in Fig.23 (a). The cohesive zone interface is located in between vertical and horizontal section as shown in Fig.16. In this study, the vertical section considered as the substrate to be optimized, measures 0.5×0.5 mm^2 and is meshed with 2500 elements. The horizontal section, a deformable region with dimensions 1×0.3 mm^2, is meshed with 3000 elements and linear graded interface region of thickness 0.01mm is discretized with 50 elements. A vertical point load P, is applied at top right corner of the deformable region. For numerical analysis the substrate, deformable and linear graded interface region properties are set same to previous peeling test problem.

Two cases were examined to study the topology evolution of the substrate under different far-field imposed displacements of 9 mm and 24 mm respectively. The topology optimization process, as outlined in Fig.11, was applied. Preliminary investigation reveals that volume fraction $f = 50\%$ is not able to provide feasible optimized design structure. The material discontinuity in the substrate region makes it unsuitable to achieve the desired structural performance. Therefore the volume fraction $f = 60\%$ is considered for analysis. The total displacement of 9 mm and 24 mm leads to delamination of 0.14 mm and 0.2 mm respectively. Hence the toplogy evolution and optimized substrate region pattern is different as one can observe from Figs.17 and 18 respectively.

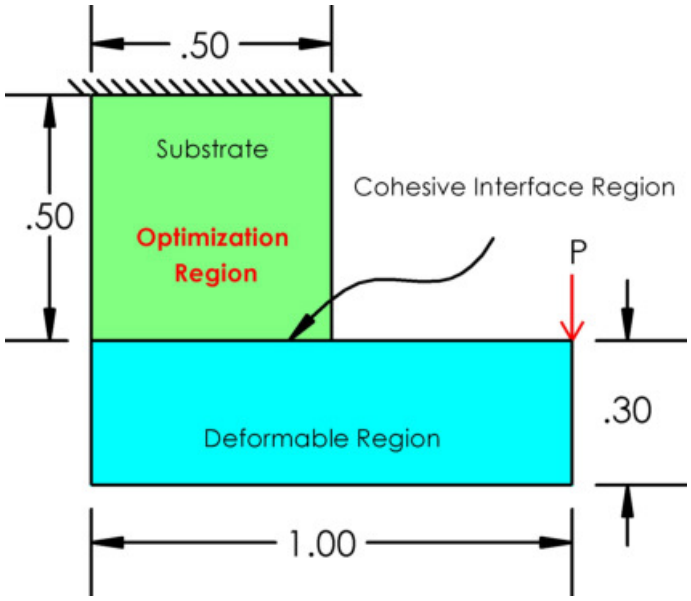

fig. 16. Sketch of L-shape structure with boundary condition and loading for a substrate with a delaminating interface, where the topology of the substrate has to be optimized to maximize the stiffness of the mechanical system for different levels of delamination.

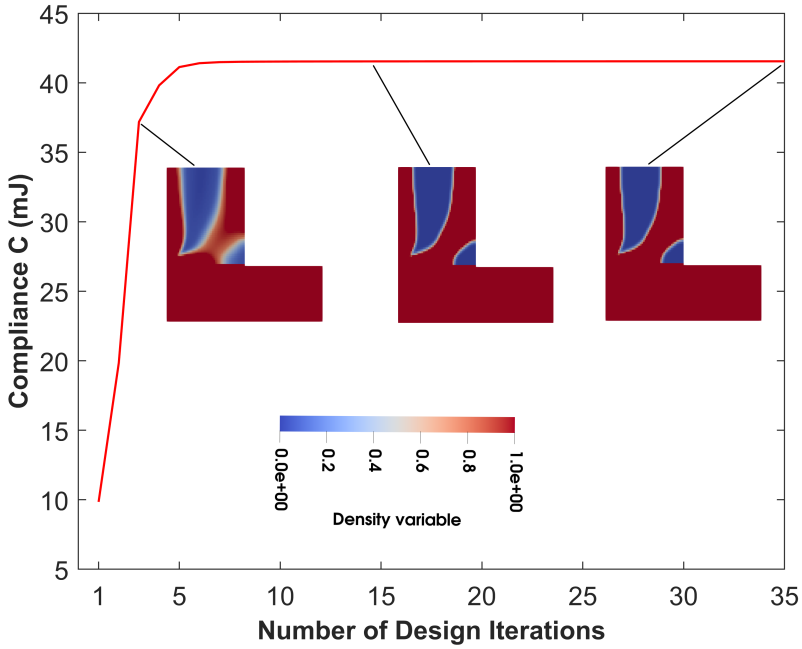

fig. 17. L-shape structural topology evolution of the substrate section for an interface with initial debonding of 0.14 mm.

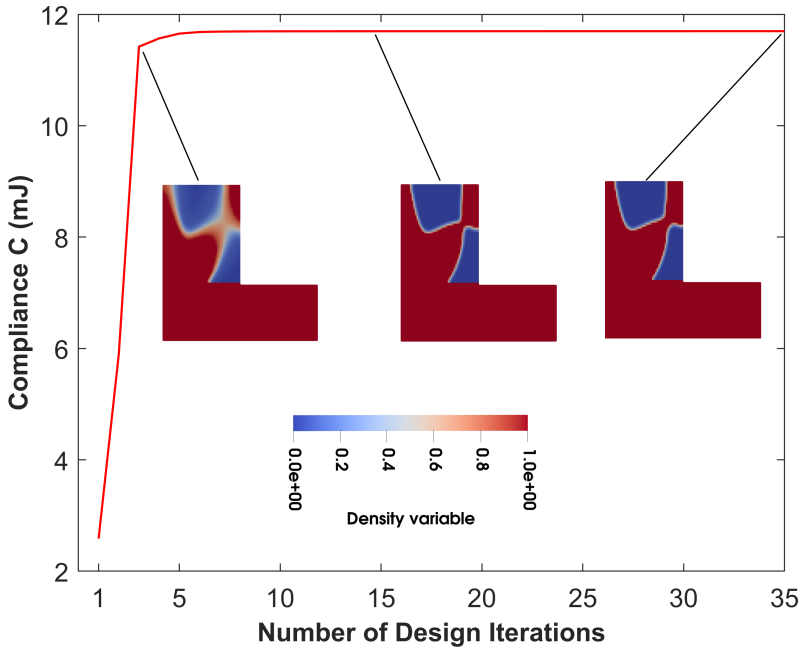

fig. 18. L-shape structural topology evolution of the substrate section for an interface with initial debonding of 0.2 mm.

5. Conclusion

In this work, structures that can be subject to delamination have been analyzed in reference to two methods to improve their mechanical response. Considering a non-linear cohesive interface model described by the Tvergaard CZM as a typical model traction-separation law, we investigated the possibility to design cohesive interfaces with a linear variation in the fracture properties along the interface, to improve resistance to peeling. This novel solution, which is nowadays technically feasible by exploiting micro-structured adhesives, has been investigated by framing the problem within an inverse analysis, where the extremal values of the fracture energy are considered as design variables. The application of the data-driven heuristic optimization approach based on PSO algorithm allowed to identify optimal values of the fracture properties in order to match a target mechanical response. The obtained solution is found to overtake the response of an interface with a uniform average interface fracture energy. The future scope of work is to work on more complex problems by conducting experiments on curvilinear adhesive bonding structures. Then, perform numerical validation for identification of cohesive zone model physical parameters using machine learning models to predict accurately the underlying physics of the problem.

The second aspect that has been considered regards the design of substrates that might have a topology optimized to withstand the onset of delamination. In this case, the optimal topology has been found by applying the physics-based mathematical approach that relies on a density-based optimization algorithm to be approached using the gradient-based optimality criteria (OC) method. The continuous design density variable adopted the solid isotropic material with penalization (SIMP) approach, along with a density filtering scheme implemented to avoid non-locality and checkboard patterns, according to the state of the art. In the test problem herein analyzed, a linearly graded interface binds the substrate and the deformable layer, and a peeling displacement is applied to delaminate a certain portion of the CZI region, considering extensions compatible with an onset of debonding. The substrate topology has been identified for two cases with different amount of delamination, and results have shown that the identified optimal topology of the substrate is mildly dependent upon the extension of the onset of debonding, which gives good perspectives on the possibility to optimize the internal material to maximize the stiffness of the system in case of potential delamination events. Furthermore, the effect of volume fraction on the optimized substrate topology is investigated and reported in identifying the best structural volume fraction optimized design. The results reported in this study contribute to the knowledge of structural mechanics, particularly for engineers and researchers working in composite materials or structures bonded with adhesives.

6. Appendix: Benchmark tests for structural topology optimization

The results of a series of benchmark tests well-known in the literature used to test the structural topology optimization algorithm. The considered problems are related

to beams with different constraints and loads, all discretized with 120×40 finite elements. The results in terms of compliance vs. number of iterations are shown in the figures below, see Figs. 19, 20, 21 and 22. Finally the method is applied to an L-geometry in Fig.23.

For all the benchmark problems, a filtered radius $r_{\min} = 2$ mm, a Young modulus $E_0 = 210$ GPa, a Poisson ratio $\nu = 0.3$ and a Young modulus $E_{\min} = 1 \times 10^{-9}$ assigned to void regions are considered. The constrained volumetric fraction f has been set equal to 0.5. The compliance decreases with respect to the number of design iterations and converges to a minimal value. The optimized topology of the structure is greatly affected by boundary conditions and it is correctly predicted as in the related literature [69, 65, 70]. The principal stress distribution for each optimum structural topology has been highlighted, where red and black colors refer to tensile or compressive stresses, respectively. Principal stress distribution diagrams might be useful and can be converted to STL (Standard Triangle Language) file format, which can be exploited for 3D printing operations.

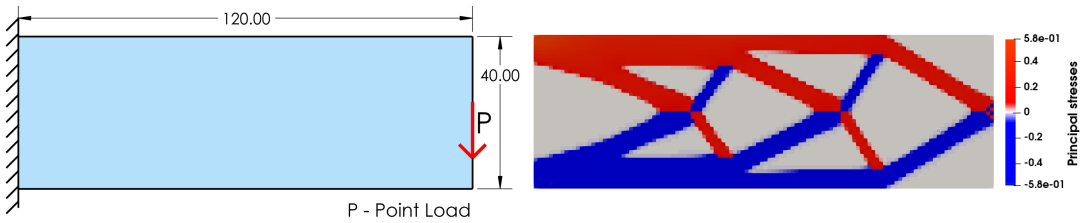

(a) Geometry

(b) Principal stresses : Red color - Tension, black color - Compression

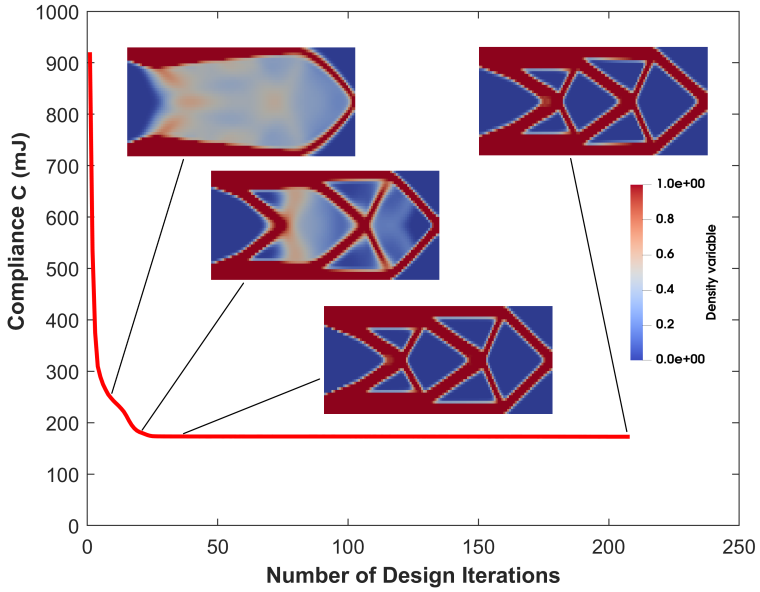

(c) Compliance versus Number of design iterations

fig. 19. Structural topology evolution of cantilever beam subjected to point load

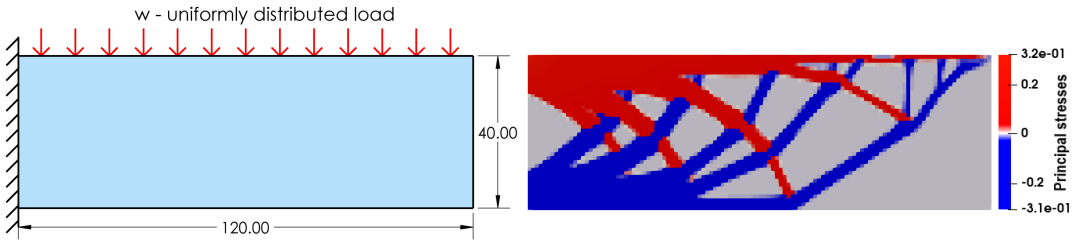

(a) Geometry

(b) Principal stresses : Red color - Tension, black color - Compression

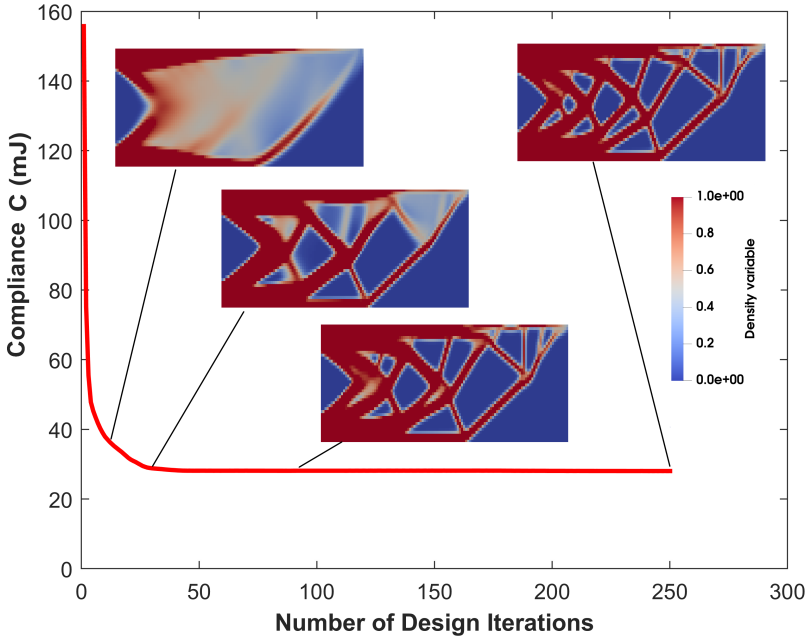

(c) Compliance versus Number of design iterations

fig. 20. Structural topology evolution of cantilever beam subjected to uniformly distributed load

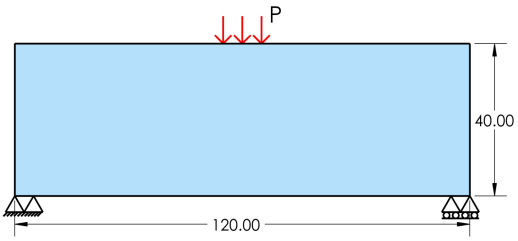

(a) Geometry

(b) Principal stresses : Red color - Tension, black color - Compression

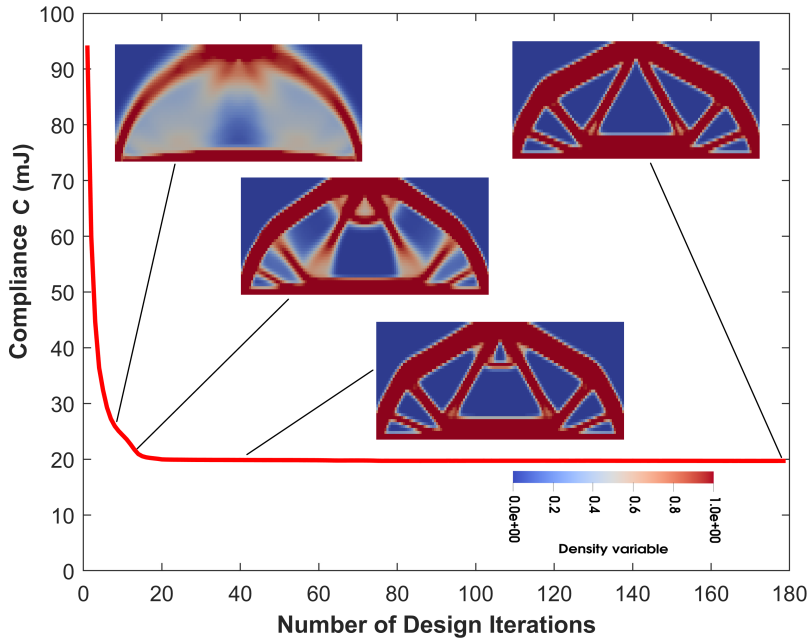

(c) Compliance versus Number of design iterations

fig. 21. Structural topology evolution of simple supported beam subjected to point load

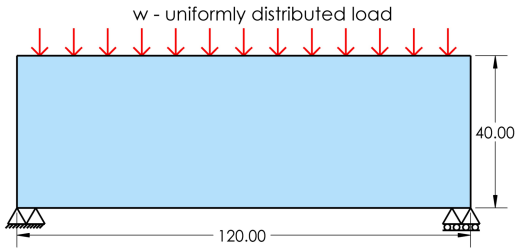

(a) Geometry

(b) Principal stresses : Red color - Tension, black color - Compression

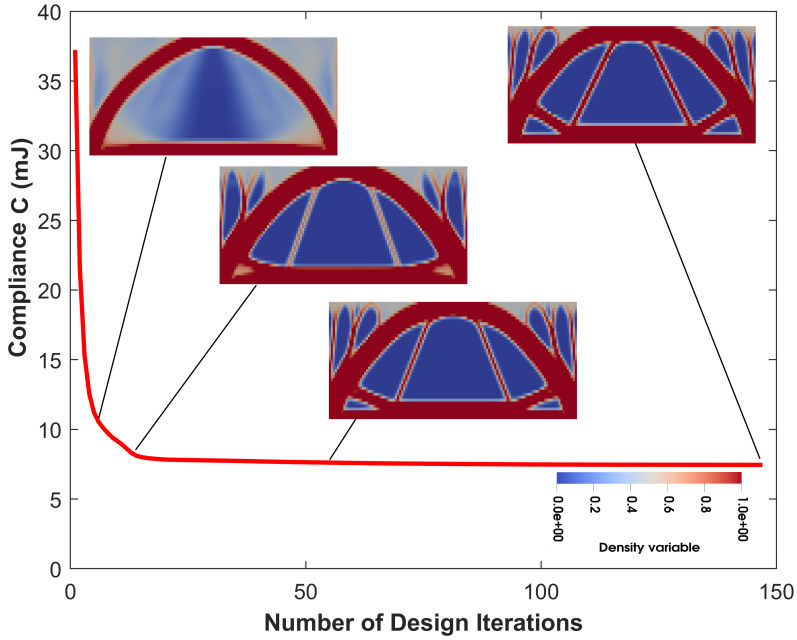

(c) Compliance versus Number of design iteration

fig. 22. Structural topology evolution of simple supported beam subjected to uniformly distributed load

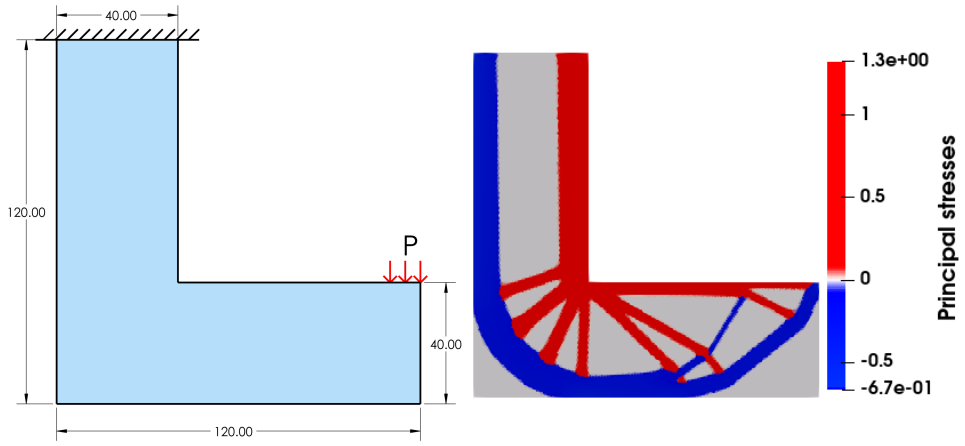

(a) Geometry

(b) Principal stresses : Red color - Tension, black color - Compression

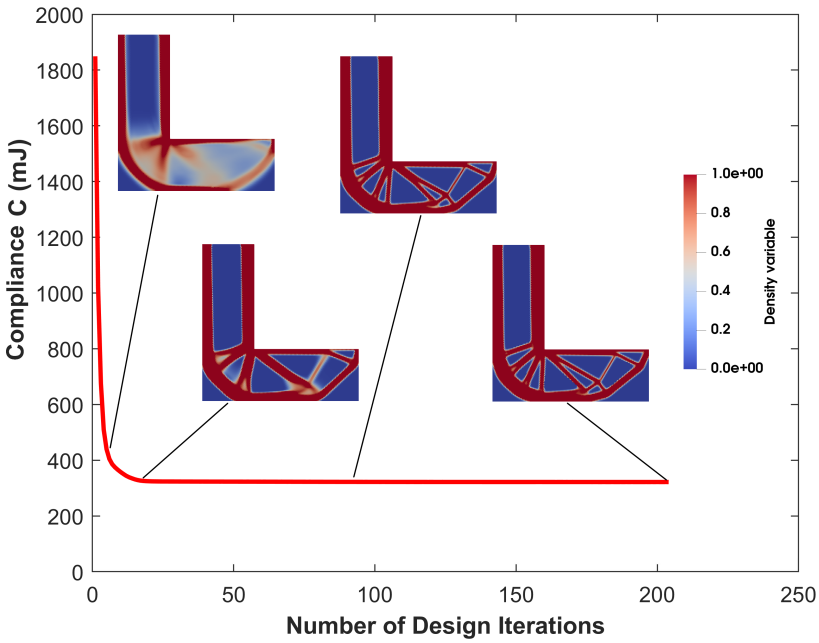

(c) Compliance versus Number of design iteration

fig. 23. Structural topology evolution of L-bracket subjected to point load

Disclosure Statement

The authors declare that they have no known competing financial interests or personal relationships that could have appeared to influence the work reported in this paper.

References

[1] A. Gent, Adhesion and strength of viscoelastic solids. is there a relationship between adhesion and bulk properties?, Langmuir 12 (19) (1996) 4492–4496. doi:https://doi.org/10.1021/la950887q.

[2] Y. Wang, G. Nian, X. Yang, Z. Suo, Lap shear of a soft and elastic adhesive, Mechanics of Materials 158 (2021) 103845. doi:https://doi.org/10.1016/j.mechmat.2021.103845.

[3] G. Barenblatt, The mathematical theory of equilibrium cracks in brittle fracture, Advances in Applied Mechanics 7 (1962) 55–129. doi:https://doi.org/10.1016/S0065-2156(08)70121-2.

[4] M. Ortiz, Y. Leroy, A. Needleman, A finite element method for localized failure analysis, Computer Methods in Applied Mechanics and Engineering 61 (2) (1987) 189–214. doi:https://doi.org/10.1016/0045-7825(87)90004-1.

[5] V. Tvergaard, Effect of fibre debonding in a whisker-reinforced metal, Materials Science and Engineering: A 125 (2) (1990) 203–213. doi:https://doi.org/10.1016/0921-5093(90)90170-8.

[6] C. Shet, N. Chandra, Effect of the shape of t–δ cohesive zone curves on the fracture response, Mechanics of Advanced Materials and Structures 11 (3) (2004) 249–275. doi:https://doi.org/10.1080/15376490490427207.

[7] D. Kaelble, Theory and analysis of peel adhesion: bond stresses and distributions, Transactions of the Society of Rheology 4 (1) (1960) 45–73. doi:10.1088/0022-3727/8/13/005.

[8] K. Kendall, Thin-film peeling-the elastic term, Journal of Physics D: Applied Physics 8 (13) (1975) 1449. doi:10.1088/0022-3727/8/13/005.

[9] Y.-Y. Su, X.-L. Gao, An analytical study on peeling of an adhesively bonded joint based on the timoshenko beam theory, Mechanics of Advanced Materials and Structures 20 (6) (2013) 454–463. doi:https://doi.org/10.1080/15376494.2011.646055.

[10] A. Molinari, G. Ravichandran, Peeling of elastic tapes: effects of large deformations, pre-straining, and of a peel-zone model, The Journal of Adhesion 84 (12) (2008) 961–995. doi:https://doi.org/10.1080/00218460802576995.

[11] M. Van den Bosch, P. Schreurs, M. Geers, A cohesive zone model with a large displacement formulation accounting for interfacial fibrilation, European Journal of Mechanics-A/Solids 26 (1) (2007) 1–19. doi:https://doi.org/10.1016/j.euromechsol.2006.09.003.

[12] J. Reinoso, M. Paggi, A consistent interface element formulation for geometrical and material nonlinearities, Computational Mechanics 54 (2014) 1569–1581. doi:https://doi.org/10.1007/s00466-014-1077-2.

[13] G. Mariggiò, J. Reinoso, M. Paggi, M. Corrado, Peeling of thick adhesive interfaces: The role of dynamics and geometrical nonlinearity, Mechanics Research Communications 94 (2018) 21–27. doi:https://doi.org/10.1016/j.mechrescom.2018.08.018.

[14] H. Zarei, M. R. Marulli, M. Paggi, R. Pietrogrande, C. Üffing, P. Weißgraeber, Mechanical characterization and failure modes in the peeling of adhesively bonded strips from a plastic substrate, Mechanics of Advanced Materials and Structures 29 (11) (2022) 1523–1528. doi:https://doi.org/10.1080/15376494.2020.1827099.

[15] L. M. Fernández-Cañadas, I. Ivañez, S. Sanchez-Saez, E. J. Barbero, Effect of adhesive thickness and overlap on the behavior of composite single-lap joints, Mechanics of Advanced Materials and Structures 28 (11) (2021) 1111–1120. doi:https://doi.org/10.1080/15376494.2019.1639086.

[16] S. Akpinar, İ. Hacısalihoglu, A. Çalık, The effect of geometry on joint strength in adhesively bonded joints with the same adhesive area, Mechanics of Advanced Materials and Structures 31 (12) (2024) 2635–2647. doi:https://doi.org/10.1080/15376494.2022.2162641.

[17] M. Paggi, P. Wriggers, Node-to-segment and node-to-surface interface finite elements for fracture mechanics, Computer Methods in Applied Mechanics and Engineering 300 (2016) 540–560. doi:https://doi.org/10.1016/j.cma.2015.11.023.

[18] J.-Y. Wu, V. P. Nguyen, A length scale insensitive phase-field damage model for brittle fracture, Journal of the Mechanics and Physics of Solids 119 (2018) 20–42. doi:https://doi.org/10.1016/j.jmps.2018.06.006.

[19] J.-Y. Wu, T. K. Mandal, V. P. Nguyen, A phase-field regularized cohesive zone model for hydrogen assisted cracking, Computer Methods in Applied Mechanics and Engineering 358 (2020) 112614. doi:https://doi.org/10.1016/j.cma.2019.112614.

[20] W.-X. Chen, J.-Y. Wu, Phase-field cohesive zone modeling of multi-physical fracture in solids and the open-source implementation in comsol multiphysics, Theoretical and Applied Fracture Mechanics 117 (2022) 103153. doi:https://doi.org/10.1016/j.tafmec.2021.103153.

[21] A. Dusane, P. Budarapu, A. Pradhan, S. Natarajan, J. Reinoso, M. Paggi, Simulation of bridging mechanisms in complex laminates using a hybrid pf-czm

method, Mechanics of Advanced Materials and Structures 29 (28) (2022) 7743–7771. doi:https://doi.org/10.1080/15376494.2021.2006835.

[22] A. Farrokhabadi, H. Madadi, M. Naghdinasab, A. Rafie, S. A. Taghizadeh, M. Herráez, Micromechanical investigation of cross-ply carbon composite laminates with glass microtubes using czm and xfem, Mechanics of Advanced Materials and Structures 29 (26) (2022) 5624–5636. doi:https://doi.org/10.1080/15376494.2021.1961177.

[23] L. Heepe, S. Gorb, Biologically inspired mushroom-shaped adhesive microstructures, Annu. Rev. Mater. Res. 44 (2014) 173–203. doi:https://doi.org/10.1146/annurev-matsci-062910-100458.

[24] S. Gorb, M. Varenberg, A. Peressadko, J. Tuma, Biomimetic mushroom-shaped fibrillar adhesive microstructure, J. R. Soc. Interface 4 (2007) 271–275. doi:https://doi.org/10.1098/rsif.2006.0164.

[25] Y. Tian, N. Pesika, H. Zeng, K. Rosenberg, B. Zhao, P. McGuiggan, K. Autumn, J. Israelachvili, Adhesion and friction in gecko toe attachment and detachment, Proceedings of the National Academy of Sciences 103 (51) (2006) 19320–19325. doi:https://doi.org/10.1073/pnas.0608841103.

[26] M. Marulli, L. Heepe, S. Gorb, M. Paggi, A finite element framework for the simulation of bio-inspired adhesives with mushroom-shaped microstructures, Mechanics Research Communications 125 (2022). doi:10.1016/j.mechrescom.2022.103963.

[27] N. Pugno, E. Lepore, S. Toscano, F. Pugno, Normal adhesive force-displacement curves of living geckos, Journal of Adhesion 87 (2011) 1059–1072. doi:https://doi.org/10.1080/00218464.2011.609439.

[28] L. Gong, D. Pan, X. Wang, Finite element modeling of the viscoelastic contact for a composite micropillar, Mechanics of Advanced Materials and Structures 28 (5) (2021) 537–549. doi:https://doi.org/10.1080/15376494.2019.1578011.

[29] K. Ni, Q. Shao, K. Wang, Z. Wang, Theoretical optimization of functional graded micropillars for strong and durable bioinspired dry adhesion, Mechanics of Advanced Materials and Structures 29 (28) (2022) 7723–7731. doi:https://doi.org/10.1080/15376494.2021.2006375.

[30] D. Whitley, A genetic algorithm tutorial, Statistics and Computing 4 (1994) 65–85. doi:https://doi.org/10.1007/BF00175354.

[31] J. Kennedy, R. Eberhart, Particle swarm optimization, in: Proceedings of ICNN'95-international conference on neural networks, Vol. 4, IEEE, 1995, pp. 1942–1948. doi:10.1109/ICNN.1995.488968.

[32] A. Gandomi, X.-S. Yang, A. Alavi, Cuckoo search algorithm: a metaheuristic approach to solve structural optimization problems, Engineering with Computers 29 (2013) 17–35. doi:https://doi.org/10.1007/s00366-011-0241-y.

[33] W. Beluch, Evolutionary identification and optimization of composite structures, Mechanics of Advanced Materials and Structures 14 (8) (2007) 677–686. doi:https://doi.org/10.1080/15376490701673250.

[34] C. Wei, J. Zhang, K. M. Liechti, C. Wu, Data driven modeling of interfacial traction–separation relations using a thermodynamically consistent neural network, Computer Methods in Applied Mechanics and Engineering 404 (2023) 115826. doi:https://doi.org/10.1016/j.cma.2022.115826.

[35] S. Ferdousi, Q. Chen, M. Soltani, J. Zhu, P. Cao, W. Choi, R. Advincula, Y. Jiang, Characterize traction–separation relation and interfacial imperfections by data-driven machine learning models, Scientific Reports 11 (1) (2021) 14330. doi:https://doi.org/10.1038/s41598-021-93852-y.

[36] A. Jaillon, J. Jumel, F. Lachaud, E. Paroissien, Mode i cohesive zone model parameters identification and comparison of measurement techniques based on uncertainty estimation, International Journal of Solids and Structures 191 (2020) 577–587. doi:https://doi.org/10.1016/j.ijsolstr.2019.12.014.

[37] S. Zhao, T. An, Q. Wang, F. Qin, Using machine learning and finite element analysis to extract traction-separation relations at bonding wire interfaces of insulated gate bipolar transistor modules, Materials 17 (5) (2024) 1002. doi:10.3390/ma17051002.

[38] D. Chen, Y. Li, X. Yang, W. Jiang, L. Guan, Efficient parameters identification of a modified gtn model of ductile fracture using machine learning, Engineering Fracture Mechanics 245 (2021) 107535. doi:https://doi.org/10.1016/j.engfracmech.2021.107535.

[39] J. Zhang, J. Zhang, D. Cao, Genetic algorithm optimization for cohesive zone modeling of viscoelastic asphalt mixture fracture based on scb test, Engineering Fracture Mechanics 271 (2022) 108663. doi:https://doi.org/10.1016/j.engfracmech.2022.108663.

[40] A. De Morais, A. Pereira, M. De Moura, F. Silva, N. Dourado, Bilinear approximations to the mixed-mode i–ii delamination cohesive law using an inverse method, Composite Structures 122 (2015) 361–366. doi:https://doi.org/10.1016/j.compstruct.2014.11.058.

[41] T. Shi, M. Pang, Y. Wang, Y. Zhang, Inverse parameter identification framework for cohesive zone models based on multi-island genetic algorithm, Engineer-

ing Fracture Mechanics 300 (2024) 110005. doi:https://doi.org/10.1016/j.engfracmech.2024.110005.

[42] V. Carollo, D. Piga, C. Borri, M. Paggi, Identification of elasto-plastic and non-linear fracture mechanics parameters of silver-plated copper busbars for photovoltaics, Engineering Fracture Mechanics 205 (2019) 439–454. doi:https://doi.org/10.1016/j.engfracmech.2018.11.014.

[43] T. Rakesh Kumar, M. Paggi, A robust identification procedure for phase field fracture mechanics parameters, Theoretical and Applied Fracture Mechanics 127 (2023) 104005. doi:https://doi.org/10.1016/j.tafmec.2023.104005.

[44] R. Behrou, M. Lawry, K. Maute, Level set topology optimization of structural problems with interface cohesion, International Journal for Numerical Methods in Engineering 112 (8) (2017) 990–1016. doi:https://doi.org/10.1002/nme.5540.

[45] A. Clausen, N. Aage, O. Sigmund, Topology optimization of coated structures and material interface problems, Computer Methods in Applied Mechanics and Engineering 290 (2015) 524–541. doi:https://doi.org/10.1016/j.cma.2015.02.011.

[46] F. Fernandes, R. Pavanello, Topology optimization of adhesive material in a single lap joint using an evolutionary structural optimization method and a cohesive zone model as failure criterion, Proceedings of the Institution of Mechanical Engineers, Part L: Journal of Materials: Design and Applications 236 (4) (2022) 757–778. doi:https://doi.org/10.1177/14644207211056945.

[47] P. Liu, Y. Luo, Z. Kang, Multi-material topology optimization considering interface behavior via xfem and level set method, Computer Methods in Applied Mechanics and Engineering 308 (2016) 113–133. doi:https://doi.org/10.1016/j.cma.2016.05.016.

[48] M. Bendsøe, N. Kikuchi, Generating optimal topologies in structural design using a homogenization method, Computer Methods in Applied Mechanics and Engineering 71 (2) (1988) 197–224. doi:https://doi.org/10.1016/0045-7825(88)90086-2.

[49] M. Bendsøe, O. Sigmund, Material interpolation schemes in topology optimization, Archive of Applied Mechanics 69 (1999) 635–654. doi:https://doi.org/10.1007/s004190050248.

[50] J. Sethian, A. Wiegmann, Structural boundary design via level set and immersed interface methods, Journal of Computational Physics 163 (2) (2000) 489–528. doi:https://doi.org/10.1006/jcph.2000.6581.

[51] Y. Xie, G. Steven, A simple evolutionary procedure for structural optimization, Computers & structures 49 (5) (1993) 885–896. doi:https://doi.org/10.1016/0045-7949(93)90035-C.

[52] Q. Li, G. Steven, Y. Xie, A simple checkerboard suppression algorithm for evolutionary structural optimization, Structural and Multidisciplinary Optimization 22 (2001) 230–239. doi:https://doi.org/10.1007/s001580100140.

[53] K. Svanberg, The method of moving asymptotes—a new method for structural optimization, International Journal for Numerical Methods in Engineering 24 (2) (1987) 359–373. doi:https://doi.org/10.1002/nme.1620240207.

[54] O. Sigmund, A 99 line topology optimization code written in matlab, Structural and multidisciplinary optimization 21 (2) (2001) 120–127. doi:https://doi.org/10.1007/s001580050176.

[55] H. Ruan, Y. Xu, J. Chen, L. Liang, X. Ju, Biomimicry and topology optimization for adhesive toughness design in bonded heterogeneous films, International Journal of Adhesion and Adhesives 132 (2024) 103684. doi:https://doi.org/10.1016/j.ijadhadh.2024.103684.

[56] P. Kumar, P. Li, J. Reinoso, Q.-C. He, J. Yvonnet, M. Paggi, SIMP Phase-field topology optimization framework to maximize fracture resistance in FGMs, Composite Structures 329 (2024) 117750. doi:https://doi.org/10.1016/j.compstruct.2023.117750.

[57] R. L. Taylor, Feap-a finite element analysis program (2014).
URL http://projects.ce.berkeley.edu/feap

[58] H. Baaser, Development and application of the finite element method based on Matlab, Springer Science & Business Media, 2010. doi:https://doi.org/10.1007/978-3-642-13153-0.

[59] O. Rabinovitch, Debonding analysis of fiber-reinforced-polymer strengthened beams: Cohesive zone modeling versus a linear elastic fracture mechanics approach, Engineering Fracture Mechanics 75 (10) (2008) 2842–2859. doi:https://doi.org/10.1016/j.engfracmech.2008.01.003.

[60] T. Bäck, H.-P. Schwefel, An overview of evolutionary algorithms for parameter optimization, Evolutionary Computation 1 (1) (1993) 1–23. doi:10.1162/evco.1993.1.1.1.

[61] R. Rao, Jaya: A simple and new optimization algorithm for solving constrained and unconstrained optimization problems, International Journal of Industrial Engineering Computations 7 (1) (2016) 19–34. doi:10.5267/j.ijiec.2015.8.004.

[62] M. Clerc, The swarm and the queen: towards a deterministic and adaptive particle swarm optimization, in: Proceedings of the 1999 congress on evolutionary computation-CEC99 (Cat. No. 99TH8406), Vol. 3, IEEE, 1999, pp. 1951–1957. doi:10.1109/CEC.1999.785513.

[63] R. Eberhart, Y. Shi, Comparing inertia weights and constriction factors in particle swarm optimization, in: Proceedings of the 2000 congress on evolutionary computation. CEC00 (Cat. No. 00TH8512), Vol. 1, IEEE, 2000, pp. 84–88. doi:10.1109/CEC.2000.870279.

[64] M. Bendsøe, Optimal shape design as a material distribution problem, Structural Optimization 1 (1989) 193–202. doi:https://doi.org/10.1007/BF01650949.

[65] E. Andreassen, A. Clausen, M. Schevenels, B. Lazarov, O. Sigmund, Efficient topology optimization in matlab using 88 lines of code, Structural and Multidisciplinary Optimization 43 (2011) 1–16. doi:https://doi.org/10.1007/s00158-010-0594-7.

[66] O. Sigmund, Materials with prescribed constitutive parameters: an inverse homogenization problem, International Journal of Solids and Structures 31 (17) (1994) 2313–2329. doi:https://doi.org/10.1016/0020-7683(94)90154-6.

[67] O. Sigmund, Morphology-based black and white filters for topology optimization, Structural and Multidisciplinary Optimization 33 (4) (2007) 401–424. doi:https://doi.org/10.1007/s00158-006-0087-x.

[68] T. Bruns, D. Tortorelli, Topology optimization of non-linear elastic structures and compliant mechanisms, Computer Methods in Applied Mechanics and Engineering 190 (26-27) (2001) 3443–3459. doi:https://doi.org/10.1016/S0045-7825(00)00278-4.

[69] H. Wang, J. Liu, G. Wen, An efficient evolutionary structural optimization method for multi-resolution designs, Structural and Multidisciplinary Optimization 62 (2020) 787–803. doi:https://doi.org/10.1007/s00158-020-02536-0.

[70] E. Biyikli, A. To, Proportional topology optimization: a new non-sensitivity method for solving stress constrained and minimum compliance problems and its implementation in matlab, PloS one 10 (12) (2015) e0145041. doi:https://doi.org/10.1371/journal.pone.0145041.